The Astrophysical Journal Letters, 929:L7 (6pp), 2022 April 10 https://doi.org/10.3847/2041-8213/ac61e0

A BL Lacertae Object at a Cosmic Age of 800 Myr

Ekaterina Koptelova and Chorng-Yuan Hwang
Graduate Institute of Astronomy, National Central University, Taoyuan City, 32001, Taiwan; koptelova@astro.ncu.edu.tw
Received 2021 December 27; revised 2022 March 15; accepted 2022 March 28; published 2022 April 11

Abstract

We report the discovery of the BL Lacertae object FIRST J233153.20+112952.11 at redshift >6 using near-infrared spectroscopy and broadband observations in the infrared, submillimeter, and radio wavelengths. The detection of the continuum break at ∼0.92 μm in the near-infrared spectrum of FIRST J233153.20+112952.11 provides an approximate redshift of 6.57, corresponding to an age of the universe of ∼800 Myr. The rest-frame UV/optical spectrum of FIRST J233153.20+112952.11 shows no emission lines detected with equivalent width >1.5 Å. The nondetection of the C IV λ1549 broad emission line constrains the luminosity of the accretion disk to be $\lesssim 10^{45}$ erg s^{-1}, which corresponds to the radiatively inefficient accretion regime of BL Lacertae objects. The spectral index of the rest-frame UV/optical continuum, $\alpha_{\nu,\mathrm{opt}} = 1.43 \pm 0.23$, is consistent with the expected spectral index of the synchrotron emission spectrum of the relativistic jet. The flat radio continuum ($\alpha_{\nu,r} \approx 0$) in a rest-frame frequency interval of 7–23 GHz is similar to that of the typical BL Lacertae objects and also consistent with originating from the synchrotron jet emission. The rest-frame UV/optical and radio fluxes of FIRST J233153.20+112952.11 show significant (15%–40%) variations. The shortest recorded rest-frame timescale of these variations is ∼8 days. Assuming the local scaling relation between the radio luminosity and black hole mass, the 5 GHz radio luminosity of FIRST J233153.20+112952.11, 1.6×10^{33} erg s^{-1} Hz^{-1}, suggests a billion solar mass central supermassive black hole.

Unified Astronomy Thesaurus concepts: Galaxies (573); Galaxy evolution (594); High-redshift galaxies (734); Active galaxies (17); Active galactic nuclei (16); Blazars (164); BL Lacertae objects (158); Radio jets (1347); Supermassive black holes (1663); Observational astronomy (1145)

1. Introduction

The BL Lacertae objects (BL Lacs) and flat-spectrum radio quasars (FSRQs), known as blazars, are radio-loud active galactic nuclei (AGNs) with relativistic jets pointed at small viewing angles to the line of sight (Urry & Padovani 1995). The BL Lacs and FSRQs usually harbor massive ($\sim 10^9\,M_\odot$) supermassive black holes (SMBHs) accreting in the radiatively inefficient regime below 1% of the Eddington luminosity (e.g., Cavaliere & D'Elia 2002; O'Dowd et al. 2002; Ghisellini et al. 2011; Shaw et al. 2013) and at the near Eddington luminosity (e.g., Ghisellini et al. 2010, 2011; Ackermann et al. 2017), respectively. The BL Lacs and FSRQs differ in the radiation power of their jets, which correlates with the luminosity of the accretion disk and is lower for BL Lacs than for FSRQs (Ghisellini et al. 2014; Paliya et al. 2020a). Unlike FSRQs, the optical spectra of BL Lacs show no broad emission lines (or only weak lines of EW < 5 Å; e.g., Stickel et al. 1991).

In the evolutionary scenario of blazars, BL Lacs are believed to represent the final evolutionary phase of FSRQs, during which SMBHs accrete at low rates due to the deficit of gas available for their growth (Cavaliere & D'Elia 2002; Ghisellini et al. 2011; Ajello et al. 2014). At low redshifts, the evolutionary connection between BL Lacs and FSRQs is suggested by their similar redshift distributions (e.g., Giommi et al. 2012; Marchã & Caccianiga 2013). Ajello et al. (2014) found that luminous BL Lacs evolve as strongly as FSRQs showing a peak in their space density at $z \sim 1.2$. Note that low-luminosity BL Lacs, which are more numerous than FSRQs at low redshifts, show negative cosmological evolution (Giommi et al. 2012; Ajello et al. 2014). The most distant FSRQs have been discovered at $z \sim 6$ (Romani et al. 2004; Frey et al. 2015; Belladitta et al. 2020), and the most distant radio-loud quasar was recently found at $z = 6.8$ (Bañados et al. 2021). At these redshifts, the universe was much denser than at the present epoch. Frequent interactions between galaxies and the gaseous environment of these high-redshift quasars favor high accretion rates and rapid accumulation of mass by SMBHs. For this reason, the high-redshift population of blazars is likely represented mainly by FSRQs. Evolutionarily older BL Lacs, if also formed at early cosmic epochs, are probably extremely rare. The most distant BL Lac currently known is J1219+3653 at $z = 3.6$ (Paliya et al. 2020b).

In this Letter, we report the first observation of a BL Lac object at a redshift of 6.57, FIRST J233153.20+112952.11 (hereafter J2331+11). It was identified by matching z_{PS1}-band dropouts from the Panoramic Survey Telescope and Rapid Response System 1 (PS1; Chambers et al. 2016) with the radio sources detected in the Faint Images of the Radio Sky at Twenty cm (FIRST; White et al. 1997; Helfand et al. 2015). Here we assume a flat cosmology with Hubble constant $H_0 = 70$ km s^{-1} Mpc^{-1}, mass density $\Omega_{\mathrm{m}} = 0.3$, and vacuum density $\Omega_\Lambda = 0.7$.

2. Observations

2.1. Broadband Data

Object J2331+11 was independently detected in the y_{PS1} band of the PS1 survey, the near- and mid-infrared bands of the United Kingdom Infrared Telescope (UKIRT) Infrared Deep Sky Survey Large Area Survey (UKIDSS LAS; Lawrence et al.

Table 1
Multiepoch Photometry of J2331+11

Survey/ Telescope	Obs. Date (yy-mm-dd)	Filter	$\lambda_{\rm eff}$ (μm)	$m_{\rm AB}$ (AB mag)
PS1	2011–2014	$z_{\rm PS1}$	0.87	>22.30 (5σ)
UKIRT	2020-11-03	Z	0.88	>22.95 (5σ)
UKIRT	2021-11-01	Z	0.88	22.71 ± 0.29
PS1	2011–2014	$y_{\rm PS1}$	0.96	21.20 ± 0.17
UKIDSS	2009-09-03	Y	1.03	21.80 ± 0.52
UKIRT	2020-11-03	Y	1.03	21.64 ± 0.16
UKIRT	2021-11-01	Y	1.03	21.46 ± 0.09
UKIDSS	2009-09-03	J	1.25	21.15 ± 0.30
UKIRT	2020-11-03	J	1.25	21.07 ± 0.12
UKIRT	2021-11-01	J	1.25	20.93 ± 0.05
UKIDSS	2009-11-03	H	1.63	20.00 ± 0.15
UKIRT	2020-11-03	H	1.63	20.57 ± 0.10
UKIRT	2021-11-01	H	1.63	20.50 ± 0.06
UKIDSS	2009-11-03	K	2.20	19.91 ± 0.13
UKIRT	2020-11-03	K	2.20	20.05 ± 0.09
UKIRT	2021-11-01	K	2.20	20.11 ± 0.09
WISE	2010–2017	W1	3.35	19.38 ± 0.04
WISE	2010–2017	W2	4.60	19.14 ± 0.07
WISE	2010–2011	W3	11.56	>17.07 (2σ)
WISE	2010–2011	W4	22.09	>15.64 (2σ)

2007) and Wide-field Infrared Survey Explorer (WISE; Wright et al. 2010; Mainzer et al. 2011), at 3 GHz of the Very Large Array Sky Survey (VLASS; during campaigns VLASS1.1 in 2017 and VLASS2.1 in 2020; Lacy et al. 2020), at 1.4 GHz of the FIRST survey (White et al. 1997; Helfand et al. 2015), at 1.4 GHz of the National Radio Astronomy Observatory Very Large Array Sky Survey (NVSS; Condon et al. 1998), and at 888 MHz of the Rapid Australian Square Kilometre Array Continuum Survey (RACS; McConnell et al. 2020). The recent near-infrared images of J2331+11 were obtained with the UKIRT telescope on 2020 November 3 and 2021 November 1 (see Tables 1 and 2).

In Table 1, the UKIDSS LAS H and K magnitudes are from the Data Release 8 (DR8) source catalog. The DR8 catalog does not provide the Y and J magnitudes; these magnitudes were estimated directly from the UKIDSS LAS images. The mid-infrared W1 and W2 magnitudes were reported in the 2 yr AllWISE (Cutri et al. 2014) and deeper 5 yr unWISE (Schlafly et al. 2019) source catalogs. Table 1 provides the unWISE W1 and W2 magnitudes and AllWISE 2σ upper limits on the W3 and W4 magnitudes. The integrated flux densities in the NVSS, VLASS1.1, and VLASS2.1 bands provided in Table 2 were measured from the continuum maps, whereas the FIRST and RACS fluxes are from the catalogs of the corresponding surveys. We note that the integrated flux density of J2331+11 measured from the VLASS1.1 Quick Look image agrees with that reported in the VLASS1.1 Quick Look Catalog.[1]

Object J2331+11 was also observed in the two frequency bandwidths, 210–222 and 230–242 GHz, of the Submillimeter Array (SMA) in the subcompact configuration (synthesized beam size ~5″) on 2021 October 9. The integration time of this observation was 1 hr, reaching an integrated sensitivity over the two bandwidths of ~0.3 mJy beam^{-1}. The raw data were calibrated using the Millimeter Interferometer Reduction (MIR) software package.[2] Quasars 3C 454.3 and J2232+117 observed together with J2331+11 as gain and flux calibrators were also used to calibrate the bandpass. The integrated flux densities measured from the continuum maps centered at 216 and 236 GHz are reported in Table 2.

Table 2
Integrated Radio/Submillimeter Flux Densities of J2331+11

Survey/ Telescope	Obs. Date (yy-mm-dd)	$\nu_{\rm obs}$ (GHz)	f_ν (mJy)
RACS	2020-11-02	0.888	2.50 ± 0.07
NVSS	1996-07-04	1.4	2.26 ± 0.34
FIRST	2011-03-19	1.4	2.13 ± 0.15
VLASS1.1	2017-10-25	3.0	2.59 ± 0.25
VLASS2.1	2020-08-29	3.0	2.46 ± 0.15
SMA	2021-10-09	216	30.51 ± 1.28
SMA	2021-10-09	236	30.47 ± 1.27

2.2. Near-infrared Spectrum

The spectroscopic observations of J2331+11 were conducted on 2020 September 30 and December 24 using the Gemini Multi-Object Spectrograph (Gemini-N/GNIRS; Elias et al. 2006) in the cross-dispersed mode and a slit width of 1″. The instrument setup provided a spectral coverage of 0.85–2.5 μm and a resolution of $R \approx 500$. The total exposure time of the data was 3.75 hr. The spectra were reduced and wavelength-calibrated using the Gemini IRAF package. The telluric correction and absolute flux calibration were performed using two telluric standard stars observed at a similar airmass: HIP 109939 (spectral type A1Vn) and HIP 5310 (A3V). The signal-to-noise ratios of the resulting spectrum in the Y, J, H, and K bands are ~5, 8, 14, and 22 (Figure 1(a)).

3. Results

3.1. Redshift, Spectral Indices, and Variability

The near-infrared spectrum of J2331+11 represents a continuum that shows a flux break at ~0.921 μm. This continuum break due to neutral hydrogen absorption in the intergalactic medium usually seen in the spectra of high-redshift quasars blueward of rest-frame 1216 Å (the Gunn–Peterson trough) provides a redshift estimate of $z \approx 6.57$. The spectrum shows absorption features at $\lesssim$1.2 μm and no detected emission lines (Figure 1(a)). Taking into account the signal-to-noise ratio of the spectrum, the minimum detectable equivalent width (EW) of the C IV λ1549 emission line is estimated to be $\mathrm{EW}_{\rm min,C\,IV} = 3\sigma_{\rm EW} \approx 1.5$ Å (see Paiano et al. 2017), where $\sigma_{\rm EW}$ is the standard deviation of the distribution of EWs measured from the spectrum using a running window of 90 Å (the expected width of C IV at $z \approx 6.6$; e.g., Vanden Berk et al. 2001).

The UV/optical continuum of J2331+11 is characterized by a spectral index of $\alpha_{\nu,\rm opt} = 1.43 \pm 0.23$ ($f_\nu \propto \nu^{-\alpha_\nu}$), measured from the GNIRS spectrum between 1.27 and 2.40 μm (excluding the regions of strong atmospheric absorption). The radio spectral index, $\alpha_{\nu,r} = 0.01 \pm 0.06$, was estimated using the radio fluxes at 0.888 and 3 GHz measured quasi-

[1] The VLASS Quick Look images and catalog are available at www.cirada.ca.

[2] The MIR cookbook by C. Qi can be found at https://lweb.cfa.harvard.edu/~cqi/mircook.html.

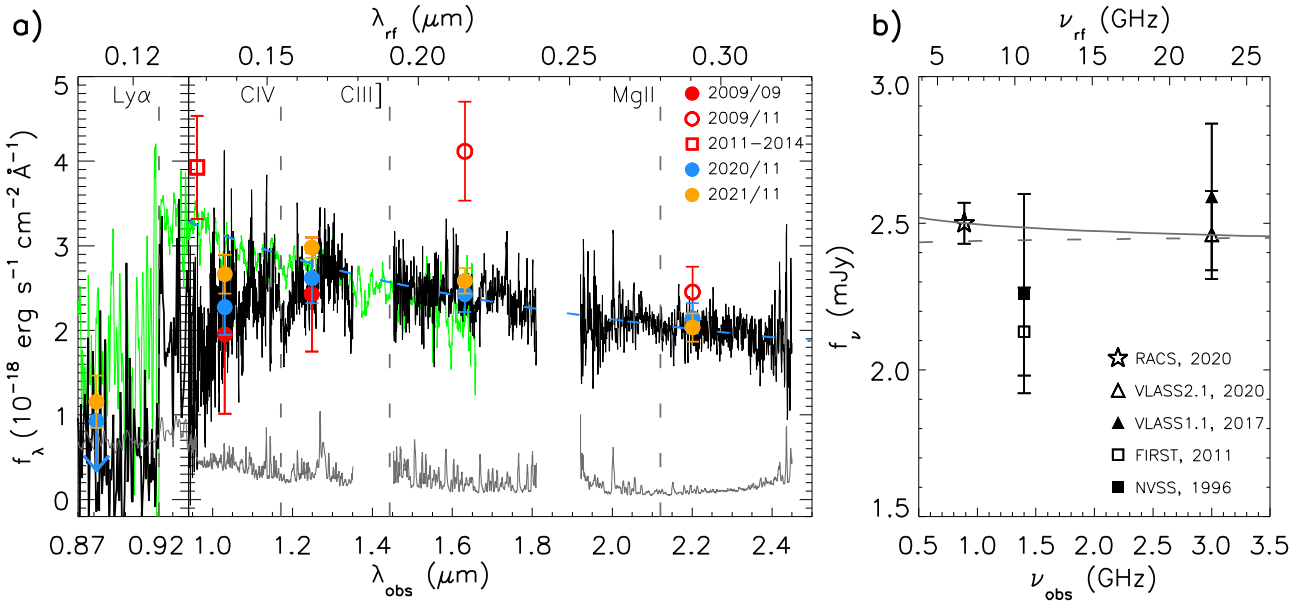

Figure 1. (a) Gemini-N/GNIRS spectrum of J2331+11 (black line). The left panel shows the enlarged view of the spectrum around the continuum break at ∼0.921 μm. The 1σ error spectrum and power law $f_\nu \propto \nu^{-1.43}$ are shown with gray and dashed blue lines. The gaps in the spectrum correspond to the regions of strong atmospheric absorption. The *Z*-, *Y*-, *J*-, *H*-, and *K*-band fluxes measured in 2020 (quasi-simultaneously with the GNIRS spectrum) and 2021 are shown with blue and orange symbols. The red symbols show the archival fluxes in the PS1 $y_{\rm PS1}$ band (open square), UKIDSS LAS *Y* and *J* (filled circles), and *H* and *K* bands (open circles). The vertical dashed lines mark the expected wavelengths of the prominent broad emission lines of quasars. The redshift-corrected SDSS spectrum of the BL Lac J1219 +36 at $z = 3.59$ (Paliya et al. 2020b) is overplotted in green for comparison. (b) Radio continuum of J2331+11. The flux measurements obtained with different instruments and at different epochs are shown with different symbols. The solid and dashed lines correspond to power laws $f_\nu \propto \nu^{-0.01}$ and $f_\nu \propto \nu^{-0.00}$ fitted to the quasi-simultaneous RACS and VLASS2.1 measurements and all multiepoch flux measurements, respectively.

simultaneously by the RACS and VLASS2.1 surveys (see Table 2 and Figure 1(b)). It was assumed that these quasi-simultaneous fluxes are less affected by variability. Additionally, the RACS and VLASS2.1 measurements are also quasi-simultaneous with the spectroscopic observations. The power-law fit to all multiepoch radio data, including the measurement by FIRST at 1.4 GHz, gives a similar value of $\alpha_{\nu,r} = 0.00 \pm 0.09$ (see Figure 1(b)). The spectral index of the radio-to-submillimeter continuum derived from the VLASS2.1 and SMA fluxes at 3 and 216 GHz is $\alpha_{\nu,\ r\text{-submm}} = -0.59 \pm 0.02$.

The quasi-simultaneous spectral energy distribution (SED) of J2331+11, constructed using the near-infrared fluxes measured in 2020, the unWISE W1 and W2 fluxes (Schlafly et al. 2019), the AllWISE upper limits on the W3 and W4 fluxes (Cutri et al. 2014), and the radio and submillimeter fluxes, was *k*-corrected using the relation $f_\nu^K = f_\nu (1+z)^{\alpha_\nu - 1}$, where f_ν is the observed flux density, α_ν is the spectral index of the local continuum, and z is the redshift of J2331+11 (see Figure 2).

The UKIDSS LAS, PS1, recent UKIRT, and Gemini-N/GNIRS data revealed significant variability of J2331+11. According to the UKIDSS LAS and PS1 photometry in the *H* and $y_{\rm PS1}$ bands, J2331+11 was $\gtrsim$0.5 mag brighter in 2009 and 2011–2014 compared to the later observations in 2020 and 2021 (see Figure 1(a) and Table 1). Additionally, the pairs of UKIDSS LAS fluxes, *Y* and *J* and *H* and *K*, measured 61 days apart, seem to correspond to the two different continuum flux levels of J2331+11. Namely, the UKIDSS *Y* and *J* fluxes are consistent with those during the UKIRT and Gemini-N/GNIRS observations in 2020–2021, whereas the UKIDSS *H* and *K* fluxes correspond to the ∼0.1–0.5 mag brighter continuum (Figure 1(a)). The continuum also shows brightening by up to $\Delta Y \approx 0.2$ mag between the UKIRT observations

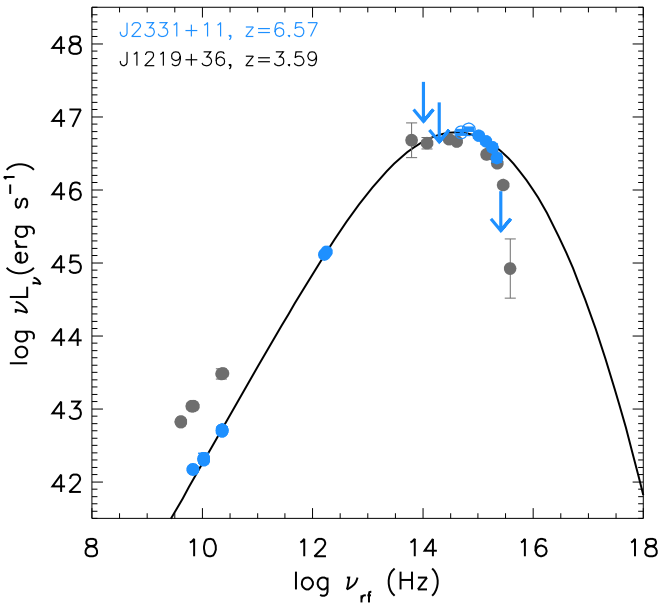

Figure 2. The SED of J2331+11. The *k*-corrected SED of J2331+11 (blue symbols) is shown in comparison with the *k*-corrected SED of the BL Lac J1219+36 at $z = 3.59$ (Paliya et al. 2020b; gray circles). The *Z*-, W3-, and W4-band flux upper limits are indicated with arrows. The black line shows the synchrotron continuum calculated using the SSC emission model.

in 2020 and 2021. The 1.4 GHz flux of J2331+11 measured by FIRST in 2011 deviates by ∼2.5σ from the flat continuum ($\alpha_{\nu,r} \approx 0$), suggesting a possible variation in the radio flux by ∼15% between 2011 and 2020 (see Table 2 and Figure 1(b)).

3.2. SED Model

The SEDs of BL Lacs exhibit two broad emission peaks (e.g., Abdo et al. 2010): the synchrotron emission peak between radio and UV/soft X-rays and the inverse Compton emission peak between hard X-rays and γ-rays. The shape of the optical-to-radio SED of J2331+11 and the lack of emission lines detected with EW > 1.5 Å resemble the properties of the synchrotron emission peak of BL Lacs. The observed SED of the distant BL Lac J1219+36 at $z = 3.59$ is shown in Figure 2 for comparison. Interestingly, J2331+11 and J1219+36 have similar peak luminosities.

The two SED peaks of BL Lacs are explained by synchrotron radiation of relativistic electrons in the jet and inverse Compton scattering of synchrotron photons on the electrons that produce them, respectively (e.g., Königl 1981). The shape of these double-peak SEDs is well described by the synchrotron self-Compton (SSC) emission model under the assumption that the emitting electrons are isotropically distributed in a homogeneous randomly oriented magnetic field (Königl 1981; Chiang & Böttcher 2002; Abdo et al. 2010; Ghisellini et al. 2011). To calculate the model of the synchrotron emission peak of J2331+11, we used the online numerical SSC code[3] (Tramacere et al. 2009). Following Abdo et al. (2010), the electron energy distribution was assumed to be log-parabolic, $n(\gamma) = K \times 10^{-r(\log(\gamma/\gamma_{\rm peak}))^2}$, where K is the normalization coefficient related to the total density of electrons N, $\gamma_{\rm peak}$ is the electron Lorentz factor at the peak of the electron energy distribution, and r is the curvature parameter of the electron energy distribution (Massaro et al. 2006; Tramacere et al. 2009; Abdo et al. 2010). The model has the following parameters: radius of the emitting region R (cm), Doppler boosting factor δ, intensity of the magnetic field B (G), curvature parameter r, electron Lorentz factor $\gamma_{\rm peak}$, and electron density $N = \int_{\gamma_{\rm min}}^{\gamma_{\rm max}} n(\gamma) d\gamma$ (cm^{-3}). As in Abdo et al. (2010), the intensity of the magnetic field and electron density were fixed to the typical values of $B \sim 0.1$ G and $N \sim 1$ cm^{-3}. Additionally, the timescale of the shortest brightness variation of J2331+11 observed by UKIDSS LAS in 2009, $t_{\rm var} \approx 61$ days, provides an estimate for the size of the emitting region of $R = ct_{\rm var}\delta/(1+z) \approx 2.1 \times 10^{17}$ cm, assuming the typical value of the Doppler factor of blazars, $\delta \approx 10$ (c is the speed of light; e.g., Tramacere et al. 2009; Abdo et al. 2010). The SED of J2331+11 is well reproduced by the SSC emission model with the following model parameters: Doppler and electron Lorentz factors of $\delta \approx 11$ (for a jet viewing angle of $\sim 1°$, it corresponds to a bulk Lorentz factor of $\Gamma \approx 5.6$) and $\gamma_{\rm peak} \approx 10^{3.5}$ and a curvature parameter of the electron distribution of $r \approx 2.2$ (see Figure 2).

4. Discussion

4.1. Emission Mechanism

The lack of detected emission lines in the spectrum of J2331+11 suggests that the thermal emission of the accretion disk is weak. The nondetected C IV line with EW > 1.5 Å provides an upper limit on the C IV line luminosity of $L_{\rm C\,IV} \lesssim 1.6 \times 10^{43}$ erg s^{-1}, smaller than the $L_{\rm C\,IV} \simeq 10^{44.5\pm0.3}$ erg s^{-1} measured for quasars (Shen et al. 2011). Assuming that the luminosity of the accretion disk is a factor of 10 greater than the luminosity of the broad-line region, $L_{\rm BLR} \approx 8.8 L_{\rm C\,IV}$ (e.g., Ghisellini et al. 2011; Paliya et al. 2020b), the 3σ upper limit on the disk luminosity of J2331+11 is $L_{\rm d} \sim 1.4 \times 10^{45}$ erg s^{-1}. As discussed in Ghisellini et al. (2011), when the luminosity of the accretion disk drops to $\lesssim 10^{45}$ erg s^{-1}, accretion becomes radiatively inefficient, corresponding to the accretion regime of BL Lacs.

The good fit of the SSC emission model to the SED of J2331+11 suggests that the observed emission is strongly dominated by the Doppler-boosted synchrotron emission of the jet. According to this model, the observed flux νf_ν of J2331+11 is expected to be amplified by >10,000 times (a factor of δ^4) compared to the intrinsic (unbeamed) flux (e.g., Ajello et al. 2014). The estimated Lorentz factor, $\Gamma \approx 5.6$, is consistent with the average bulk Lorentz factor of BL Lacs from the γ-ray ($\Gamma \approx 6$; Ajello et al. 2014) and radio ($\Gamma \approx 10$; Hovatta et al. 2009) observations. The synchrotron continuum of the SSC emission model reaches a peak luminosity of $L^{\rm syn}_{\rm peak} \approx 10^{46.79}$ erg s^{-1} at a rest-frame frequency of $\nu^{\rm syn}_{\rm peak} \approx 10^{14.58}$ Hz, corresponding to ~ 0.79 μm. Thus, the energy of the synchrotron emission peak of J2331+11 is similar to the energy of the intermediate synchrotron peaked BL Lacs, defined as those showing synchrotron peaks at 10^{14}–10^{15} Hz (Abdo et al. 2010).

The UV/optical spectral index of J2331+11, $\alpha_{\nu,\rm opt} = 1.43 \pm 0.23$, agrees within the uncertainty with a spectral index of $\alpha^{\rm syn}_{\nu,\rm opt} = 3/2$ predicted by the SSC emission model in the UV/optical wavelengths (e.g., Chiang & Böttcher 2002). For comparison, the thermal emission of the accretion disks of normal and weak-line quasars is characterized by a flatter UV/optical continuum with a spectral index of ~ 0.44 (Vanden Berk et al. 2001; Diamond-Stanic et al. 2009). The radio spectral index of J2331+11 measured at rest-frame 7–23 GHz ($\alpha_{\nu,r} = 0.01 \pm 0.06$) is similar to the typical spectral indices of blazars, which show the flat radio continuum dominated by the synchrotron emission of the bright compact core of the jet. For comparison, the average radio spectral index of γ-ray-detected blazars within a similar rest-frame frequency range is $\langle \alpha_{\nu,r} \rangle \sim 0.03 \pm 0.23$ (Abdo et al. 2010). The radio continua of normal and weak emission line quasars are usually steeper than those of blazars (e.g., Diamond-Stanic et al. 2009; Belladitta et al. 2020).

Blazars are among the most variable AGNs. Their variability is closely related to the emission mechanism and the properties of the emitting region. The injection of fresh electrons accelerated to higher energies than the previously injected cooled electrons causes the synchrotron continua of BL Lacs to evolve to higher intensities and peak frequencies, i.e., to show the bluer-when-brighter behavior (e.g., Isler et al. 2017). During the brightening of 2009, the spectral index of the UV/optical continuum of J2331+11 became flatter, $\alpha_{\nu,\rm opt} \sim 0.27$, and the H–K color became bluer by ~ 0.4 mag, as expected for the jet-driven brightness variations. The higher amplitudes of the brightness changes in the bluer bands than in the redder bands observed between 2020 and 2021 ($\Delta Y \approx 0.18$, $\Delta J \approx 0.14$, $\Delta H \approx 0.07$, and $\Delta K \approx -0.06$ mag) also agree with the jet-driven variations.

4.2. Radio Luminosity–SMBH Mass

The radio luminosity of J2331+11 at rest-frame 5 GHz is $L_{\rm 5GHz} = 4\pi D_{\rm L}^2 f^{\rm obs}_{\rm 888\,MHz}(1+z)^{\alpha_{\nu,r}-1} \approx 1.6 \times 10^{33}$ erg s^{-1} Hz^{-1} (where $f^{\rm obs}_{\rm 888\,MHz}$ is the observed radio flux at 888 MHz, which is close to rest-frame 5 GHz, and $\alpha_{\nu,r} \approx 0$ is the measured radio spectral index). This radio luminosity is

[3] https://tools.ssdc.asi.it/SED/

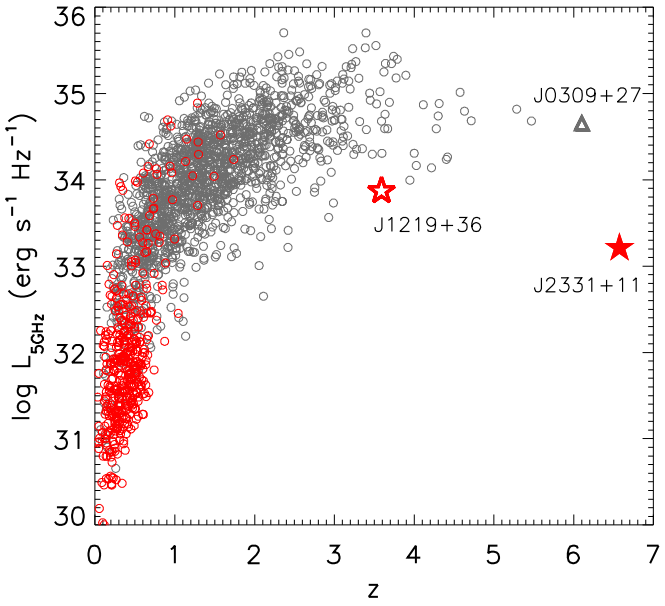

Figure 3. Radio luminosity of blazars vs. redshift. The black and red open circles depict FSRQs and BL Lacs from the fifth edition of the ROMA-BZCAT multifrequency catalog of blazars (Massaro et al. 2015). The red filled star shows J2331+11. The high-redshift BL Lac J1219+36 at $z = 3.59$ (Paliya et al. 2020b) and the most distant FSRQ currently known, J0309+27 at $z = 6.10$ (Belladitta et al. 2020), are shown with an open star and a triangle, respectively.

comparable to those of luminous BL Lacs at low redshifts, which are relatively rare, <1 in Gpc^3 (see Figure 3; Stickel et al. 1991; Marchã & Caccianiga 2013).

The 5 GHz luminosities and masses of the SMBHs of low-redshift BL Lacs estimated using stellar velocity dispersions correlate approximately as $L_{5\ \mathrm{GHz}} \propto M_{\mathrm{BH}}^{0.63}$ (León-Tavares et al. 2011). This relation predicts that the mass of the SMBH of J2331+11 is in the range of $(7\text{–}174) \times 10^9\ M_\odot$, where the range limits correspond to the intrinsic 1σ scatter of the relation of ± 0.7 dex.

4.3. Formation Timescale

The growth rates of the SMBHs of BL Lacs are extremely low compared to those of quasars. Ghisellini et al. (2011) defined the accretion rate below which the accretion regime of FSRQs changes to that of BL Lacs to be $L_{\mathrm{BLR}}/L_{\mathrm{Edd}} = 5 \times 10^{-4}$, or $L_{\mathrm{d}}/L_{\mathrm{Edd}} \approx 5 \times 10^{-3}$ (where $L_{\mathrm{Edd}} = 1.26 \times 10^{38} (M_{\mathrm{BH}}/M_\odot)$ erg s^{-1} is the Eddington luminosity). The limits on M_{BH} and L_{d} obtained in Sections 4.1 and 4.2 imply $L_{\mathrm{d}}/L_{\mathrm{Edd}} \sim (0.1\text{–}1.6) \times 10^{-3}$, further suggesting that J2331+11 is likely in the accretion regime of a BL Lac. The black hole of an initial mass of $10^6\ M_\odot$ accreting at $L_{\mathrm{d}}/L_{\mathrm{Edd}} \lesssim 0.1$ and ~1 would grow into a $10^9\ M_\odot$ SMBH on timescales of $\gtrsim 3$ and ~0.3 Gyr, respectively (Madau et al. 2014). In order to reach a mass of $10^9\ M_\odot$ by an age of the universe of 0.8 Gyr, the SMBH of J2331+11 should have been grown at an accretion rate of $\gtrsim 1$ during the FSRQ phase. Some of the known high-redshift quasars, including the radio-loud quasar at $z = 6.8$, do show such high accretion rates (e.g., Koptelova et al. 2019; Bañados et al. 2021). Without continuous gas replenishment, the timescale of the Eddington-limited growth of SMBHs is relatively short, ~0.1 Myr (Yu et al. 2013). Thus, the transition of J2331+11 from the FSRQ to BL Lac phase might have happened on timescales of $\gtrsim$0.1 Myr, whereas its SMBH should have already been on the order of $10^9\ M_\odot$ during the FSRQ phase at $z > 6.57$. Moreover, J2331+11 implies the presence of up to $2\Gamma^2 \approx 200$ (assuming $\Gamma \sim 10$) similar objects at $z \gtrsim 6.57$ with $\sim 10^9\ M_\odot$ SMBHs but randomly oriented jets, which might have a similar formation mechanism and timescale.

Further observations of J2331+11, in particular the high-resolution observation of its radio structure with very long baseline interferometry (similar to those of a few known high-redshift blazars; e.g., Frey et al. 2015), will be crucial for its further investigation.

This work was supported by the Ministry of Science and Technology of Taiwan, grant Nos. MOST 109-2112-M-008-021-MY3 and MOST 110-2112-M-008-021-MY3. Based on data obtained at the international Gemini Observatory, a program of NSF's NOIRLab, via the time exchange program between Gemini and the Subaru Telescope (Program ID: GN-2020B-FT-109). The Subaru Telescope is operated by the National Astronomical Observatory of Japan. The international Gemini Observatory at NOIRLab is managed by the Association of Universities for Research in Astronomy (AURA) under a cooperative agreement with the National Science Foundation on behalf of the Gemini Observatory partnership: the National Science Foundation (United States), National Research Council (Canada), Agencia Nacional de Investigación y Desarrollo (Chile), Ministerio de Ciencia, Tecnología e Innovación (Argentina), Ministério da Ciência, Tecnologia, Inovações e Comunicações (Brazil), and Korea Astronomy and Space Science Institute (Republic of Korea). Based on observations obtained with UKIRT (Program IDs: U/20B/NCU02, U/21B/NCU01) and SMA (Project ID: 2021A-A012). UKIRT is owned by the University of Hawaii (UH) and operated by the UH Institute for Astronomy; operations are enabled through the cooperation of the East Asian Observatory. The Submillimeter Array is a joint project between the Smithsonian Astrophysical Observatory and the Academia Sinica Institute of Astronomy and Astrophysics and is funded by the Smithsonian Institution and the Academia Sinica.

ORCID iDs

Ekaterina Koptelova https://orcid.org/0000-0002-7477-0206
Chorng-Yuan Hwang https://orcid.org/0000-0002-3658-0903

References

Abdo, A. A., Ackermann, M., Agudo, I., et al. 2010, ApJ, 716, 30
Ackermann, M., Ajello, M., Baldini, L., et al. 2017, ApJL, 837, L5
Ajello, M., Romani, R. W., Gasparrini, D., et al. 2014, ApJ, 780, 73
Bañados, E., Mazzucchelli, C., Momjian, E., et al. 2021, ApJ, 909, 80
Belladitta, S., Moretti, A., Caccianiga, A., et al. 2020, A&A, 635, L7
Cavaliere, A., & D'Elia, V. 2002, ApJ, 571, 226
Chambers, K. C., Magnier, E. A., Metcalfe, N., et al. 2016, arXiv:1612.05560
Chiang, J., & Böttcher, M. 2002, ApJ, 564, 92
Condon, J. J., Cotton, W. D., Greisen, E. W., et al. 1998, AJ, 115, 1693
Cutri, R. M., Wright, E. L., Conrow, T., et al. 2014, yCat, 2328, 0
Diamond-Stanic, A. M., Fan, X., Brandt, W. N., et al. 2009, ApJ, 699, 782
Elias, J. H., Joyce, R. R., Liang, M., et al. 2006, Proc. SPIE, 6269, 62694C
Frey, S., Paragi, Z., Fogasy, J. O., & Gurvits, L. I. 2015, MNRAS, 446, 2921
Ghisellini, G., Della Ceca, R., Volonteri, M., et al. 2010, MNRAS, 405, 387
Ghisellini, G., Tavecchio, F., Foschini, L., & Ghirlanda, G. 2011, MNRAS, 414, 2674

Ghisellini, G., Tavecchio, F., Maraschi, L., Celotti, A., & Sbarrato, T. 2014, Natur, 515, 376
Giommi, P., Padovani, P., Polenta, G., et al. 2012, MNRAS, 420, 2899
Helfand, D. J., White, R. L., & Becker, R. H. 2015, ApJ, 801, 26
Hovatta, T., Valtaoja, E., Tornikoski, M., & Lähteenmäki, A. 2009, A&A, 494, 527
Isler, J. C., Urry, C. M., Coppi, P., et al. 2017, ApJ, 844, 107
Königl, A. 1981, ApJ, 243, 700
Koptelova, E., Hwang, C.-Y., Malkan, M. A., & Yu, P.-C. 2019, ApJ, 882, 144
Lacy, M., Baum, S. A., Chandler, C. J., et al. 2020, PASP, 132, 035001
Lawrence, A., Warren, S. J., Almaini, O., et al. 2007, MNRAS, 379, 1599
León-Tavares, J., Valtaoja, E., Chavushyan, V. H., et al. 2011, MNRAS, 411, 1127
Madau, P., Haardt, F., & Dotti, M. 2014, ApJL, 784, L38
Mainzer, A., Bauer, J., Grav, T., et al. 2011, ApJ, 731, 53
Marchã, M. J. M., & Caccianiga, A. 2013, MNRAS, 430, 2464
Massaro, E., Tramacere, A., Perri, M., Giommi, P., & Tosti, G. 2006, A&A, 448, 861
Massaro, E., Maselli, A., Leto, C., et al. 2015, Ap&SS, 357, 75
McConnell, D., Hale, C. L., Lenc, E., et al. 2020, PASA, 37, e048
O'Dowd, M., Urry, C. M., & Scarpa, R. 2002, ApJ, 580, 96
Paiano, S., Landoni, M., Falomo, R., et al. 2017, ApJ, 837, 144
Paliya, V. S., Ajello, M., Cao, H.-M., et al. 2020a, ApJ, 897, 177
Paliya, V. S., Domínguez, A., Cabello, C., et al. 2020b, ApJL, 903, L8
Romani, R. W., Sowards-Emmerd, D., Greenhill, L., & Michelson, P. 2004, ApJL, 610, L9
Schlafly, E. F., Meisner, A. M., & Green, G. M. 2019, ApJS, 240, 30
Shaw, M. S., Romani, R. W., Cotter, G., et al. 2013, ApJ, 764, 135
Shen, Y., Richards, G. T., Strauss, M. A., et al. 2011, ApJS, 194, 45
Stickel, M., Padovani, P., Urry, C. M., Fried, J. W., & Kuehr, H. 1991, ApJ, 374, 431
Tramacere, A., Giommi, P., Perri, M., Verrecchia, F., & Tosti, G. 2009, A&A, 501, 879
Urry, C. M., & Padovani, P. 1995, PASP, 457, 803
Vanden Berk, D. E., Richards, G. T., Bauer, A., et al. 2001, AJ, 122, 549
White, R. L., Becker, R. H., Helfand, D. J., & Gregg, M. D. 1997, ApJ, 475, 479
Wright, E. L., Eisenhardt, P. R. M., Mainzer, A. K., et al. 2010, AJ, 140, 1868
Yu, P.-C., Huang, K.-Y., Hwang, C.-Y., & Ohyama, Y. 2013, ApJ, 768, 30